FI SEVIER

Contents lists available at ScienceDirect

# Science of the Total Environment

journal homepage: www.elsevier.com/locate/scitotenv



# Activation of persulfate by CoO nanoparticles loaded on 3D mesoporous carbon nitride (CoO@meso-CN) for the degradation of methylene blue (MB)



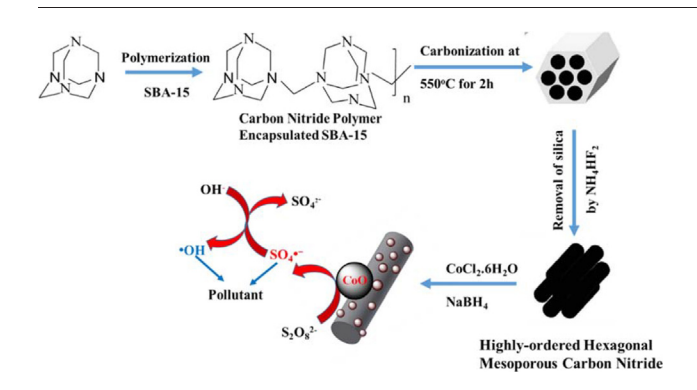
Thanh Binh Nguyen <sup>a</sup>, Ruey-an Doong <sup>b</sup>, C.P. Huang <sup>c</sup>, Chiu-Wen Chen <sup>a</sup>, Cheng-Di Dong <sup>a,\*</sup>

- <sup>a</sup> Department of Marine Environmental Engineering, National Kaohsiung University of Science and Technology, Kaohsiung City, Taiwan
- <sup>b</sup> Department of Biomedical Engineering and Environmental Sciences, National Tsing Hua University, Hsinchu 30013, Taiwan
- <sup>c</sup> Department of Civil and Environmental Engineering, University of Delaware, Newark 19716, DE, USA

### HIGHLIGHTS

- Mesoporous carbon nitride enhances persulfate activation on CoO surface.
- High initial pH is more beneficial for persulfate activation by CoO@meoso-Col
- Both SO<sub>4</sub>\* and OH• are the major reactive species for methylene blue degradation.
- The catalyst remains high activity after five-successive cycles.

### GRAPHICAL ABSTRACT



### ARTICLE INFO

Article history: Received 12 December 2018 Received in revised form 7 March 2019 Accepted 15 April 2019 Available online 18 April 2019

Editor: Bingcai Pan

Keywords:
Mesoporous carbon nitride (meso-CN)
CoO nanoparticles (CoO NPs)
Persulfate activation hazardous chemicals
Methylene blue (MB)

### ABSTRACT

A simple and facile synthesis method is developed for the fabrication of CoO loaded ordered mesoporous carbon nitride (CoO@meso-CN) composites, at various CoO loadings, and used, for the first time, to activate persulfate (PS) for methylene blue (MB) degradation. The interfacial interaction between the ultrafine CoO nanoparticles, immobilized by high surface area, regular mesopores, and graphitic nature of the meso-CN support can further enhance the catalytic activation of PS for methylene blue (MB) degradation. Among all catalysts studied, the 5-wt% CoO@meso-CN exhibits the best catalytic performance with a  $k_{\rm obs}$  of 0.264 min<sup>-1</sup>. High initial pH, especially at pH-11, is more beneficial for PS activation. Furthermore, the CoO@meso-CN nanocatalyst is highly stable with a consistently high degree of MB degradation and negligible cobalt leaching for at least 5 consecutive catalytic cycles. Both  $SO_4$ \* and OH\* are the major reactive species based on results of EPR and quenching experiments. The degradation intermediates of MB are also identified by HPLC/MS/MS and the possible degradation pathway is proposed. Results clearly demonstrate that CoO@meso-CN is a promising green catalyst with enormous potential for the remediation of hazardous chemicals using PS.

© 2019 Elsevier B.V. All rights reserved.

## 1. Introduction

Advanced oxidation technologies (AOPs), especially those based on sulfate radical ( $SO_4^{\bullet-}$ ), have received considerable attention for the

<sup>\*</sup> Corresponding author. E-mail address: cddong@mail.nkmu.edu.tw (C.-D. Dong).

destruction of recalcitrant organic contaminants (Rastogi et al., 2009; Shih et al., 2016).  $SO_4$ • has a high redox potential (2.5–3.1 V vs. NHE) and lifetime longer than OH• ( $t_{1/2} = 30-40 \mu s v s t_{1/2}, \le 1 \mu s of$ OH•), which enables excellent electron transfer and contact with target pollutants (Olmez-Hanci and Arslan-Alaton, 2013; Chen et al., 2015b). Generally, sulfate radical can be produced through the activation of persulfate (PS) by several reagents including alkaline (Lominchar et al., 2018), UV (Dhaka et al., 2017), heat (Chen et al., 2015a), activated carbon (Lee et al., 2013), and transition metals (Dong et al., 2017a). Compared with high energy-based activation methods (i.e., UV light, thermal), PS activation by transition metal catalyst, such as Co<sup>2+</sup>, Mn<sup>2</sup> +, Fe<sup>2+</sup>, Ce<sup>3+</sup> (Hu and Long, 2016) and Cu<sup>2+</sup> (Jaafarzadeh et al., 2017), is highly efficient in wastewater treatment and remediation. Among the PS activation catalysts, Co<sup>2+</sup> has been the most reactive. However, Co<sup>2+</sup>-based homogeneous catalysis has limited practical value due to the subsequent disposal of cobalt containing effluents. Note that cobalt is toxic to the ecosystem and a possible carcinogen for human (Leyssens et al., 2017). Thus, the development of heterogeneous cobalt-based catalysts has received much attention because of enhanced activity and stability in PS activation. Some heterogeneous catalysts such as cobalt oxide (Zhang et al., 2016), spinel-type ferrite (Al-Anazi et al., 2018) and immobilized cobalt (Shukla et al., 2011) are efficient for the activation of PS to generate SO<sub>4</sub>• and OH•, and thus effective for the oxidation of persistent organic contaminants.

Mesoporous carbon nitride (meso-CN) materials and their functional composites are essential to many industrial applications such as energy storage, catalysis, and adsorption and separation (Lakhi et al., 2017). In particular, the incorporation of N atoms into the C structure of meso-CN yields plentiful basic sites, in the form of amine group, on the mesoporous walls, which provides the platform for the stabilization and reduction of the nanoparticles (Datta et al., 2010). As support for metal nanoparticles in catalysis, meso-CN with both high specific surface area and large pore size/volume can not only offer a high dispersion of nanoparticles, but also facilitate electron transfer (Vinu, 2008). Furthermore, meso-CN has been successfully utilized as support to disperse and stabilize metal nanoparticles such as Pd (Elavarasan et al., 2016), Pt (Bello et al., 2017), and Au (Datta et al., 2010). Basically, meso-CN is synthesized by nanocasting method as one of the most effective and reproducible strategies for its synthesis, wherein N-containing organic chemicals and mesoporous siliceous materials are employed as precursors and sacrificial templates, respectively (Lakhi et al., 2017). In view of its unique structure and preponderance, meso-CN has been widely employed in a wide variety of fields such as oxygen reduction reaction (Kwon et al., 2012), water splitting (Mane et al., 2017), and dehydrogenation catalysis (Kahri et al., 2017), Recently, Yang et al. (2015) have reported that the nitrogen-functionalized mesoporous carbon shows

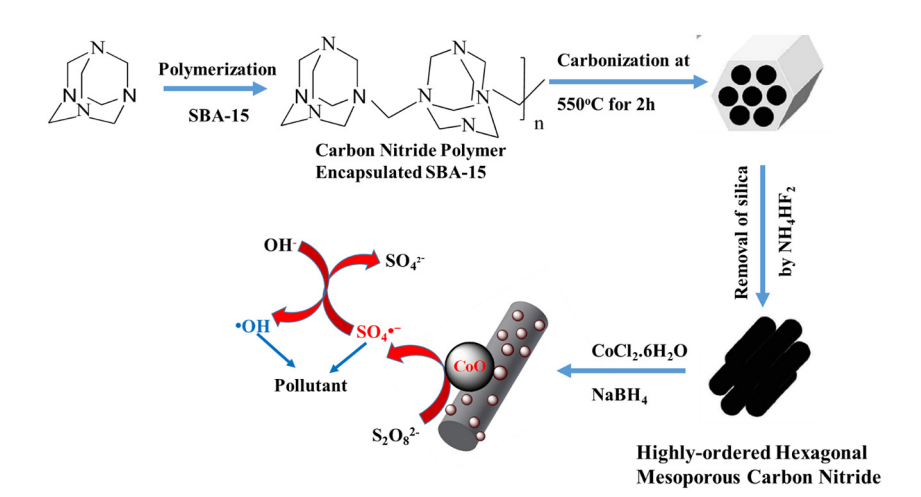
excellent adsorption capacity and good reusability for the simultaneous removal of metal ions and organic compounds. For heterogeneous catalysis processes, organic compounds and metal derivatives could bind onto the surface of meso-CN through the surface anchoring sites to improve the catalytic reaction rate, and thus broaden the catalytic application of meso-CN to organic decomposition. The unique architecture of meso-CN and the outstanding catalytic performance of CoO nanoparticles (CoO NPs) provides promising support to judiciously decorate CoO NPs for the formation of highly active and green heterogeneous catalysts. More interestingly, structurewise, CoO NPs and meso-CN are interdependent and mutually reinforcing. Up to now, the combination of CoO NPs and meso-CN as heterogeneous catalysts to activate PS reaction in organic pollutants degradation has received little attention. This has prompted us to explore the catalytic performance of CoO@meso-CN in activating PS for the rapid removal of organic contaminants, which can widen the application of CoO@meso-CN/PS to environmental remediation.

Herein, we report the synthesis of mesoporous carbon nitride (meso-CN) with ordered, uniform channel morphology for use as a supporting platform for CoO NPs. Methylene blue (MB) is a typical organic dye in wastewater and has usually been selected as a model water organic pollutant. Thus, the catalytic activity of the catalysts is examined in the activation of PS for the degradation of MB as a model compound. Scheme 1 shows the fabrication of CoO@meso-CN via chemical reduction method in the presence of NaBH<sub>4</sub> and the catalytic degradation of MB in the presence of PS. A series of experiments are conducted to reveal the effect of the catalytic system for MB degradation and mineralization. Especially, the loading content of CoO and other operating parameters such as initial pH, the concentration of PS, and primary reactive oxidants generated by CoO@meso-CN/PS system are examined. Moreover, the kinetics and the pathways for MB degradation in the CoO@meso-CN/PS system are studied. Finally, the catalytic reactions are run in five cycles to investigate the stability and reusability of CoO@meso-CN nanocatalysts for MB degradation by activated PS. To the best of our knowledge, this is the first report on the synthesis of CoO@meso-CN and subsequent test for the catalytic degradation of MB through the activation of PS.

# 2. Materials and methods

# 2.1. Materials

Pluronic P123 (( $C_3H_6O$ ). $C_2H_4O$ )<sub>x</sub>,  $M_w = 5800$ ), tetraethyl orthosilicate (TEOS) (Si $C_8H_{20}O_4$ , 98%), and sodium borohydride (NaBH<sub>4</sub>, >98%) are purchased from Sigma-Aldrich. Hexamethylenetetramine (HTM) ( $C_6H_{12}N_4$ , 99%) and ammonium hydrogen fluoride



Scheme 1. Schematic illustration of the fabrication procedure of CoO@meso-CN nanocomposites and the catalytic activation of PS by CoO@meso-CN for MB degradation.

(NH<sub>4</sub>HF<sub>2</sub>, 95%) are purchased from Alfa Aesar (UK). Methylene blue (MB) ( $C_{16}H_{18}CIN_3S$ , 99%) is purchased from Kojima Chemicals Co. (Japan). Persulfate (PS) (Na<sub>2</sub>S<sub>2</sub>O<sub>8</sub>, 98%) is purchased from Showa Chemical Industry Co. (Japan). Cobalt chloride 6-hydrate (CoCl<sub>2</sub>.6H<sub>2</sub>O,  $\geq$ 98%), hydrochloric acid (HCl, 36.5–38%), and other reagents are obtained from J. T. Baker (USA). All the chemicals are used as received without further purification.

### 2.2. Synthesis of SBA-15 template

SBA-15 is prepared according to a modified method reported previously (Dos Santos et al., 2013). Briefly, 4.0 g portion of triblock copolymer Pluronic P-123 is dissolved into a solution of 30 g of DI water and 120 g of 2 M HCl. Then, 8.50 g of TEOS is added to the above solution under vigorous stirring at 35 °C for 20 h. The resulting mixture is aged at 80 °C for 6 h. The solid product is collected by filtration, washed with DI water and ethanol, then dried in an oven at 60 °C overnight. The final product is calcined at 500 °C for 6 h in air.

### 2.3. Synthesis of meso-CN

Meso-CN is prepared using SBA-15 and hexamethylenetetramine (HTM) as template and precursor, respectively. Briefly, 8 g of HTM, dissolved in 10 g of deionized water, is used to impregnate 1 g of SBA-15 by vigorous stirring at room temperature for 5 h. Then, the mixture is centrifuged at 11,000 rpm for 5 min to remove excess HTM and the solid precipitate is dried in a 50 °C oven for 12 h. After drying, the remaining white solid (~3.8 g) is ground in a mortar. The obtained powder is then heated to 550 °C for 2 h at a ramping rate of 2 °C min $^{-1}$  under a  $\rm N_2$  flow in a tube furnace (NBD-01200, Sheng Cing Instrument Co., Taiwan). The as-synthesized dark powder is immersed in 100 mL of NH $_4$ HF $_2$  aqueous solution (4 mol L $^{-1}$ ) for 2 days to remove the siliceous template and then washed with DI water and ethanol several times. Finally, the dark sample is dried in a freeze dryer for 12 h.

# 2.4. Synthesis of CoO@meso-CN

CoO@meso-CN nanocatalyst is synthesized by immobilizing CoO NPs onto the surface of meso-CN in the presence of NaBH<sub>4</sub>. Typically, 100 mg of the as-prepared meso-CN is dispersed in 40 mL of deionized water and ultrasonicated for 30 min to obtain the homogeneous dispersion. Then 10 mL of the precursor containing CoCl<sub>2</sub>.6H<sub>2</sub>O (equivalent to 5 wt% CoO) is added to the above suspension and vigorously stirred for 30 min to enhance the interfacial interaction between meso-CN and Co<sup>2</sup> <sup>+</sup> ion at room temperature under N<sub>2</sub> atmosphere. Afterward, a large excess of NaBH<sub>4</sub> solution is added dropwise to the suspension and the mixture is stirred for 2 h at 30 °C to convert ionic Co<sup>2+</sup> to metallic Co via chemical reduction method. The mixture is further incubated for 1 h in aqueous solution to oxidize Co into CoO under normal atmosphere. According to reported results, after the reduction of Co<sup>2+</sup> ion into metallic Co with NaBH4, the spontaneous oxidation of Co into CoO in aqueous solution can easily undergo under normal air atmosphere (Bindumadhavan et al., 2016). The resultant nanocomposite is separated by filtration, washed thoroughly with deionized water several times, finally freeze-dried and stored in a glove box to minimize the further oxidation of cobalt species.

# 2.5. Experimental procedure

The catalytic oxidation of MB by CoO@meso-CN-activated PS is carried out in 50 mL-conical tubes containing 0.1 mM of MB solution. The tube is mounted on a digital rotator (MX-RD Pro, DRAGON Lab., China) and rotated at a speed of 50 rpm at room temperature (298 K). In a typical test, 10 mg catalyst is first dispersed into the MB solution and mixed for 30 min to achieve adsorption-desorption equilibrium between catalysts and MB before the addition of a certain amount of PS to

initiate the degradation reaction. The initial solution pH is adjusted by 0.1 N of NaOH or HCl. At the predetermined time interval, a water sample (1 mL) is collected with a syringe and instantaneously filtered through 0.2-µm syringe filter discs (Chromophil® Xtra H-PTFE-20/13, Germany) to remove suspended solids. Meanwhile, reactive radicals are quenched by 0.5 mL of test-butanol and ethanol (1:1, v: v) before analyzing the residual MB concentration. The concentration of MB is analyzed using a UV–vis spectrometer (Hitachi U3900) at an absorption wavelength of 660 nm. Additionally, mineralization is evaluated in terms of total organic carbon (TOC) using a Lotix combustion TOC analyzer (Teledyne Tekmar, USA). Experiments are carried out in triplicate under identical conditions and all data points are averaged.

The intermediates of MB degradation are identified using Waters Quattro Micro HPLC/MS/MS equipped with C-18 column and quadrupole tandem mass spectrometer. The mobile phase is a mixture of two solutions, namely A and B. Solution A is made of 0.1 vol% formic acid in deionized water; solution B is acetonitrile. The gradient elution is as follows: 0.5 min 90% A, 0.5–2.8 min 90% B, 2.8–3.2 min 90–60% B, 3.2–3.5 min 60–10% B and 3.5–4.5 min 10% B (Khan et al., 2014).

### 2.6. Characterization

The surface morphology of the as-synthesized materials is characterized by field emission scanning electron microscope (SEM, Hitachi SU8010) with an acceleration electron voltage of 15 kV. All samples are Pt-coated using Ion Sputter  $\epsilon$ -1030 (Hitachi, Tokyo) to increase the conductivity. High-resolution transmission electron microscopy (HRTEM) is performed using JEM-2010F (JEOL, Japan). X-ray diffraction (XRD) patterns are recorded via a Bruker D8 Advance X-ray diffractometer (Bruker, USA) with Ni-filtered Cu K $\alpha$  radiation ( $\lambda$  = 1.5406 Å) operated at a generator voltage of 40 kV and an emission current of 40 mA.

The Brunauer-Emmett-Teller (BET) specific surface area and pore size distribution are determined by nitrogen adsorption and desorption at 77 K using a surface area and porosimetry system (ASAP 2020, Micromeritics). The thermal stability of all samples is carried out using the thermogravimetric analyzer (TGA) (Mettler Toledo TGA/DSC 3+STAR) in the temperature range of 30–1000 °C (10 °C min $^{-1}$ ) under  $N_2$  (40 mL min $^{-1}$ ) to evaluate the CoO content in the sample. Raman spectra are collected using a Bruker Senterra micro-Raman spectrometer equipped with a laser power of 5 W operating at a wavelength of 532 nm. FTIR spectra are obtained by a Horiba FT-720 spectrometer at a resolution of 2 cm $^{-1}$  with KBr method. Electron paramagnetic resonance (EPR) spectra are recorded on EPR spectrometer (Bruker, EMX-10) working at X-band frequency of 9.49–9.88 GHz with a power of 8.02 mW.

The X-ray photoelectron spectroscopy (XPS) measurements are performed on an ESCA PHI 1600 photoelectron spectrometer from Physical Electronics using Al K $\alpha$  as the excitation source with a photon energy of 1486.6 eV. Zeta potential is measured by Zetasizer Nano ZS (Malvern) at 25 °C.

### 3. Results and discussion

# 3.1. Characterization of CoO@meso-CN composite

Fig. S1a shows the SEM images the CoO nanoparticles deposited onto meso-CN, which gives the structure and morphology of the catalyst. The SEM images show the presence of elongated, 330-nm-wide tubular-like particles and meso-CN consisting of many tubular-like domains with an average size of 950-nm aggregates to the wheat-like macrostructure, similar to that of parent mesoporous silica template SBA-15 (Fig. S1b). The characteristics indicate that the hexagonal mesostructure of SBA-15 is successfully replicated by meso-CN. After CoO NPs are immobilized onto the meso-CN framework, the structure and morphology of the meso-CN remain intact. However, no CoO NP is observed obviously on the surface of meso-CN by SEM, which possibly

indicates the loading of ultrasmall CoO NPs on the channels of the mesoporous carbon. The energy dispersive X-ray (EDS) spectrum (Fig. S2) further confirms the existence of carbon, nitrogen, and cobalt, and the successful deposition of CoO NPs on the external surface of meso-CN. The accurate amount of Co present in the sample is determined by inductively coupled plasma atomic spectrometry (ICP-AES) analysis, which matches well with our initial calculated amount (~5 wt%).

The TEM images are further used to confirm the size, shape, and morphology of the synthesized CoO NPs on the surface of meso-CN. Fig. 1a clearly shows the TEM image of the well-ordered porous structures of mesopores, which are similar to the mesostructured of SBA-15 in shape, suggesting a good replication. The characteristics agree well with the meso-CN synthesized in the previous work (Jun et al., 2009). Owing to the uniform mesoporous structure, there are more active sites being created and thus greater adsorption capacity is expected, which would be beneficial for CoO NPs in activating the reaction. In addition, a regular arrangement of dark spherical spots, corresponding to CoO nanoparticles, are clearly observed along the nanochannels of the support. Interestingly, linearly arranged mesochannels, in regular intervals, are also clearly seen, suggesting that the mesostructure of the support is stable even after the formation of CoO nanoparticles.

The HRTEM image (Fig. 1b) clearly shows the strong interfacial interaction between CoO NP and meso-CN, and is conducive to the electron transfer processes. The inter-fringe distance of 0.256 nm for CoO NPs is clearly shown in Fig. 1c corresponding to the (111) plane of face center cubic CoO. The orientation of these lattice fringes is similar. This suggests that the CoO NP generally grows along the CoO (111) planes. From the TEM analysis, it can be concluded that the interconnected CoO network was formed due to the reduction reaction in a mixture of Co(NO<sub>3</sub>)<sub>2</sub>, meso-CN, and NaBH<sub>4</sub>. The particle size distribution of CoO NPs on meso-CN can be calculated from the histogram analysis, and the CoO NPs on the meso-CN are in the range of 8–12.5 nm with a mean diameter of 10 nm (Fig. S3).

The structural identity and phase purity of the as-obtained meso-CN before and after the encapsulation of CoO NPs are confirmed by the

powder X-ray diffraction (PXRD) patterns, as shown in Fig. 1c. The wide-angle XRD patterns of both samples present the distinct reflections at  $2\theta = 25.5^{\circ}$  (d = 0.35 nm), corresponding to the (002) reflection plane, which is characteristic of the interplanar stacking structures of graphitic materials (Zhao et al., 2014). In the case of composite samples, the intense peak at 25.5° decreases as a result of the dilution effect. Moreover, the PXRD pattern shows one separate reflection at  $2\theta =$  $44.8^{\circ}$  (d = 0.256 nm) ascribing to the (111) planes of CoO NPs (JCPDS No. 48-1719). The peak is very broad and weak suggesting the formation of ultrasmall nanocrystalline CoO particles insides the pore channels of carbon nitride. The absence of large and intense peaks at higher angles further confirms the absence of large particles on the external surface of the support. The most intense peak positioned (2 $\theta$ ) at 44.8 is used to calculate the size of the CoO NPs in the composite. The size of the CoO nanoparticles calculated according to the Scherrer equation is ~10.3 nm, which matches well with the result of HRTEM. Fig. S4 shows the small angle patterns of meso-CN before and after the incorporation of CoO NPs. Similar to the XRD pattern of meso-CN, the CoO@ meso-CN sample also shows the strong diffraction peak (100) at  $2\theta =$ 0.96°, which indicates the retention of the intrinsic hexagonally ordered mesoporous structure (space group p6mm) (Zhao et al., 2014). Nevertheless, the intensity of the (100) peak of CoO@meso-CN is appreciably lower than that of meso-CN. This result can be attributed to the difference of scattering contrasts of the pores and the walls, and to the filling of the pores with CoO NPS, which are formed along the channels of the carbon nitride, confirming that CoO NPS are indeed coordinated to the nanochannels of the carbon nitride. These results reveal the pore-sizecontrolled growth of the nanoparticle in the confined matrix and the reduction of Co(NO<sub>3</sub>)<sub>2</sub> in the presence of by NaBH<sub>4</sub> has not changed the structure of meso-CN.

The change of the textural parameters of meso-CN after the encapsulation of the CoO NPS over the mesochannels is evaluated by nitrogen adsorption-desorption isotherm measurement (Fig. 2a). The prepared samples show classical type IV N<sub>2</sub> adsorption-desorption isotherm according to the IUPAC classification with a steep H1 hysteresis loop at

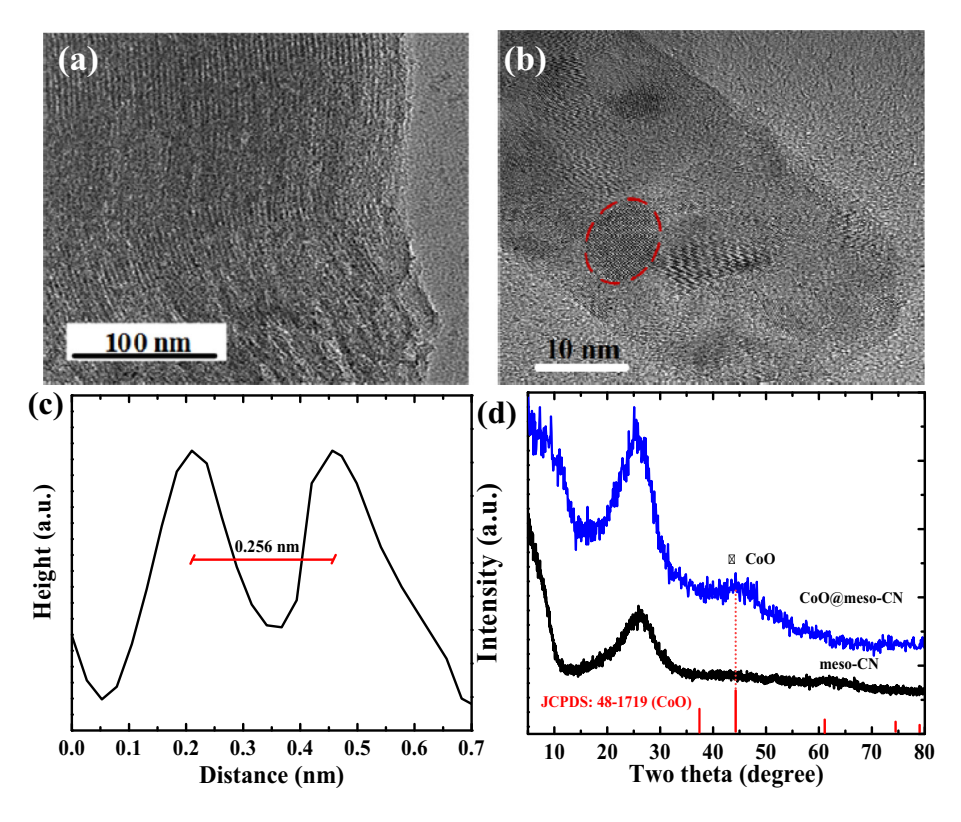


Fig. 1. (a) TEM, (b) HRTEM images of CoO@meso-CN composite, (c) lattice pattern of CoO NPs in the CoO@ meso-CN composite, and (d) XRD pattern of meso-CN and CoO@meso-CN.

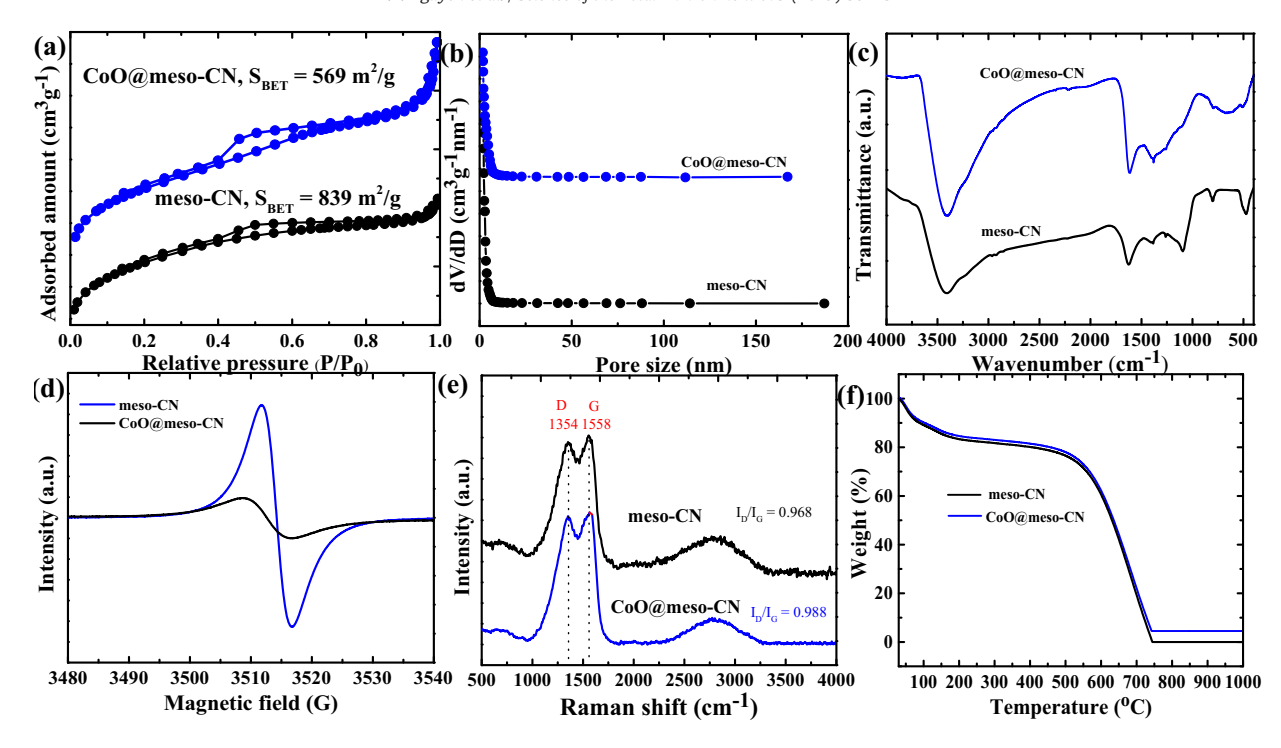


Fig. 2. (a) Nitrogen adsorption-desorption isotherms, (b) pore size distribution curves, (c) FT-IR spectra, (d) room-temperature EPR spectra, (e) Raman spectra, and (f) thermogravimetric curve for meso-CN and CoO@meso-CN samples.

 $0.2-0.85 p/p_0$ . Results indicate that the catalysts possess typically cylindrical narrow mesopores of narrow pores. The pore size distributions for the two samples obtained by the Barret-Joyner-Halenda (BJH) method reveal that the pores are highly ordered and have a narrow pore size distribution centered at 2 nm (Fig. 2b). In addition, the shape of the isotherm and the hysteresis loop of the two samples are almost identical. The results reveal that the highly ordered structure is maintained after the encapsulation of CoO nanoparticles. A small change in the specific surface area and the specific pore volume of the sample after CoO encapsulation is observed. The specific surface area is found to decrease from 839  $\text{m}^2\,\text{g}^{-1}$  for pure MCN to 569  $\text{m}^2\,\text{g}^{-1}$  for CoO nanoparticle encapsulated meso-CN, and the specific pore volume decreases from 0.52 to 0.49 cm<sup>3</sup> g<sup>-1</sup> for the same samples. The result could be mainly due to the loading of nanoparticles onto the external wall of meso-CN, demonstrating that the inbuilt basic sites or groups on the support materials do not allow the agglomeration or migration of the nanoparticles, but instead stabilize or anchor them on the pore wall structure. However, the size of the nitrogen adsorbate molecule is small enough to penetrate insides the pore channels of the support, encapsulated with the metal nanoparticles through the microporous channels connected between the primary mesopores of the support. Thus, it is also possible that the reduction of the textural parameters of the support may originate from blockage caused by the encapsulated nanoparticles with sizes slightly larger than that of the pore size of the support. Based on the above results, it is concluded that the high specific surface area, large pore volume, and unique mesoporous carbon nitride enables its use as a metal-free catalyst support.

In order to probe the chemical functionality, the meso-CN, and CoO@ meso-CN materials are characterized by FT-IR. Fig. 2c shows the transmittance spectra of the catalyst composite. A broad band at approximately 3500–3200 cm<sup>-1</sup> is attributed to the stretching vibration of N—H, and O—H bonds of adsorbed water. The presence of NH stretching vibration modes indicates that some uncondensed amine functional groups still exist in the carbon nitride layer, which can act as ligands to coordinate with metal ions and thus efficiently stabilize CoO NPs (Datta et al., 2010). Several strong bands in the range of

1200–1650 cm<sup>-1</sup> dominate the spectrum with peaks at approximately 1264, 1413, and 1616 cm<sup>-1</sup>, which correspond to the typical stretching mode of CN heterocycles. The band at 805 cm<sup>-1</sup> is characteristic of the out-of-plane bending modes of CN heterocycles of triazine units (Kroke et al., 2002). The broad band at 662 cm<sup>-1</sup> originate from the stretching vibrations of the metal-oxygen (Co—O) bonds, which is clear evidence for the presence of crystalline CoO in CoO@meso-CN composite besides the major chemical structures of meso-CN is retained after the synthetic procedure of composite.

It is known that the structure of meso-CN is originated from the formation of s-triazine units into an extended  $\pi$ -conjugated system, which depends on the extent of polymerization (Li et al., 2015). The evolution of the band structure of meso-CN before and after the introduction of CoO NPs is monitored using electron paramagnetic resonance (EPR) spectra at the room temperature (Fig. 2d). Both samples show one single Lorentzian line centering at a g value of 2.0034, originated from the unpaired electron on the  $\pi$ -conjugated meso-CN aromatic rings. In addition, the EPR intensities are greatly strengthened when adding a small amount of CoO. This demonstrates that the strong interaction between CoO and the nitrogen atoms of s-triazine subunit can effectively accelerate the electron mobility in the  $\pi$ -conjugated system of meso-CN, potentially due to the delocalization of the valance electron of CoO to the meso-CN conjugation system to facilitate charge collection and separation at the heterogeneous interface.

Raman spectroscopy is a powerful tool to evaluate the crystalline structure of carbon materials and detecting the loading effect of heteroatoms. Raman spectra of both samples exhibit two bands at around 1354 and 1558 cm $^{-1}$  corresponding to D (A1g mode) and G (E2g mode) bands, respectively (Fig. 2e). The D band stands for the degree of disorder as a defect, while the G band reflects the level of graphitization as the crystallization degree of the sp $^2$  hybrid carbon atom (Zhao et al., 2014). In the Raman spectrum of both samples, the intensity of the G band is higher than that of the D band, suggesting that many sp $^2$  hybridized carbon species are present in the graphitized pore walls and high electron conductivity of the hybrid (Zhao et al., 2014). In addition, the intensity ratio of  $I_D/I_G$  for CoO@meso-CN is 0.988, which is

higher than that of pristine meso-CN ( $I_D/I_G=0.968$ ). The increase in the disordered structure of meso-CN after loading with CoO NPs onto the surface is mainly attributed to the interaction between the graphitic backbone and the heteroatoms in the nanocomposite, which may enhance the catalytic efficiency of PS activation.

Fig. 2f shows the thermogravimetric profile of meso-CN and CoO@ meso-CN from 30 to 1000 °C in a nitrogen atmosphere. The minor loss generated at 100–140 °C in both samples is associated with the loss of physically adsorbed water. The pristine meso-CN shows the thermal stability up to 500 °C and the weight loss increases rapidly from 500 to 750 °C, indicating the sublimation and/or decomposition of meso-CN. Nearly complete decomposition of meso-CN is observed at 750 °C. Addition of CoO NPs enhances the thermal stability slightly and the weight of CoO@meso-CN nanocomposites starts to decrease at 550 °C, which is mainly due to the strong interaction between CoO NPs and the layer-stacking motif of meso-CN. The main weight loss between 550 °C and 750 °C is ascribed to the loss of meso-CN. Furthermore, the decomposition of CoO@meso-CN stops at 750 °C with a residual weight fraction of 5 wt%, which is in good agreement with the result of CoO loading obtained from ICP-AES measurement.

Above results show that in addition to the structure feature, surface compositions and chemical states of the as-prepared samples are essential. Therefore, XPS is employed to analyze the CoO, N and O chemical states of the nanocomposites. As illustrated in Fig. 3a, the full XPS survey scan spectra of both meso-CN and CoO@ meso-CN show C 1s and N 1s peaks at 288 and 399 eV, respectively. Moreover, two additional Co 2p and O 1s peaks at 782 and 531 eV, respectively, appear in CoO@meso-CN confirming the existence of CoO NPs on the surface of meso-CN. No other peaks have been observed. As can be seen in Fig. 3b, the spectrum of C 1s can be deconvoluted into three peaks with binding energies of 284.7 (C=C), C—N or (287.4) C—C, and 290.9 (C=N), respectively. The N 1s spectra of all three samples can be deconvoluted into three peaks around 398.1, 400.3, and 403.1 eV, corresponding to pyridinic N, pyrrolic N, and oxidized N, respectively (Fig. 3c). The Co 2p spectrum

(Fig. 3d) is characterized by two peaks with a binding energy of 83.2 and 87.4 eV for Co  $2p_{3/2}$  and Co  $2p_{1/2}$ , respectively, which is in good agreement with metallic Co (Yang et al., 2009). Moreover, the peak intensity of Co 2p increases with the increase in CoO content from 2 to 8 wt%, which is in good agreement with the added CoO loading.

# 3.2. Effect of CoO content on the catalytic activity of CoO@meso-CN

Fig. 4a shows the effect of mass loading of CoO in CoO@meso-CN on the catalytic activation of PS toward MB oxidation, Results show <5% MB degradation in 5 min for the control experiment, conducted only in the presence of PS. In term of unsupported CoO@meso-CN, 12% and 31% of MB is removed by adsorption and oxidation, respectively, in 15 min. However, introducing a certain amount of CoO generally enhances the removal efficiency and rate of MB over CoO@meso-CN in the presence of PS. Among the loading CoO@meso-CN composites, the 5 wt% CoO@meso-CN exhibits the highest degree of PS activation, achieving 99% MB degradation in 15 min. Meanwhile, the removal efficiency of MB is 62 and 79% for 2 and 8 wt% CoO@meso-CN, respectively.

The kinetics of MB degradation follows the pseudo-first-order equation modeled by the Langmuir-Hinshelwood mechanism. The observed rate constant ( $k_{\rm obs}$ ) can be determined from the slope of linear  $\ln(C_t/C_0)$  vs. time (t) plot, where  $C_0$  and  $C_t$  are the MB concentration at the initial (t=0) and at time t, respectively. As seen, the pseudo-first-order rate constant for MB degradation is 0.029 ( $r^2=0.993$ ), 0.055 ( $r^2=0.994$ ), 0.264 ( $r^2=0.990$ ), and 0.095  $\min^{-1}$  ( $r^2=0.993$ ), respectively, for the 0, 2, 5, and 8 wt% CoO@meso-CN (Fig. 4b). TOC removal is 12, 25, 68, and 47% in 15 min for catalysts doped with 0, 2, 5, and 8 wt% CoO@meso-CN, respectively. The results clearly demonstrate significant improvement of the catalytic activity of CoO@meso-CN in persulfate oxidation of MB compared to that of pure meso-CN. Results also indicate that the synergetic effect between CoO and meso-CN plays a key role in the MB degradation reaction. The 5 wt% CoO@meso-CN exhibits the best catalytic activity in comparison with other CoO loadings and this

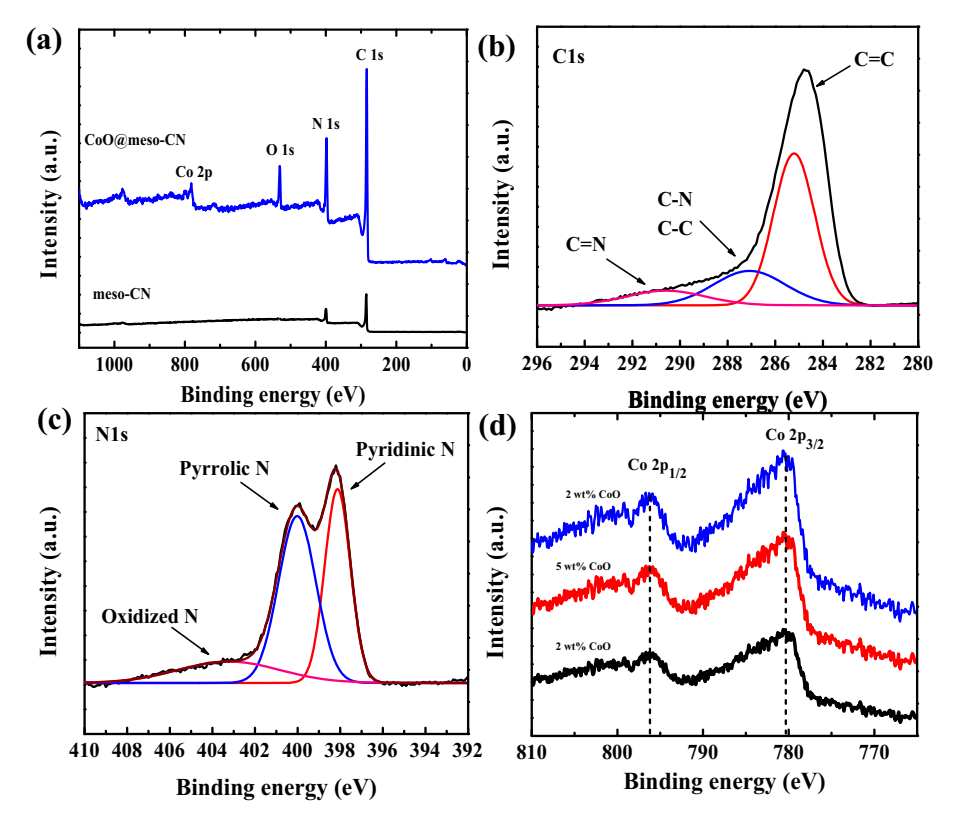


Fig. 3. XPS spectra of the as-prepared CoO@meso-CN: (a) XPS survey, (b) C 1s, (c) N 1s, and (d) Co 2p.

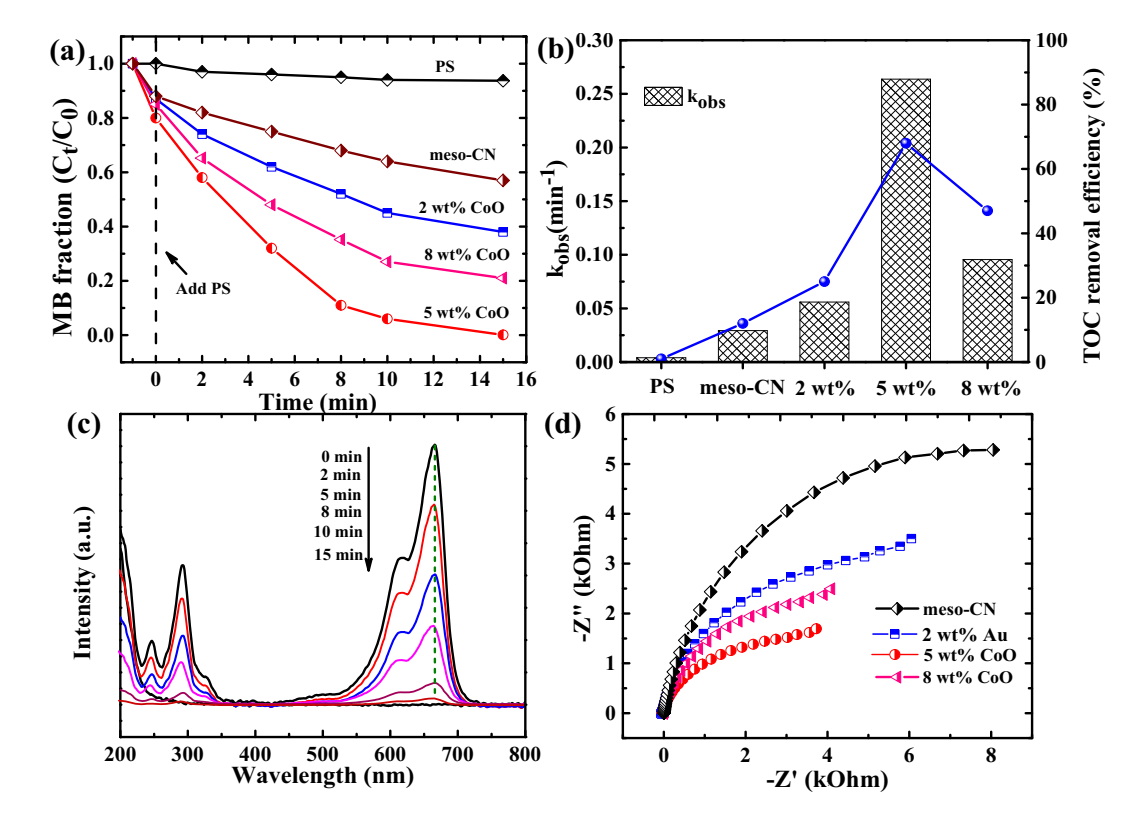
catalyst is used for further experiments. Noticeably, as shown in Table S1, the  $k_{\rm obs}$  value for MB degradation by CoO@meso-CN composite in this study is observed higher than or comparable to most of the reported data (References in Supplementary data), clearly showing that the composite is a promising material in PS activation for enhancement of the efficiency and rate of MB degradation.

Fig. 4c depicts the temporal evolution of the UV–vis spectra in the range of 200–800 nm of aqueous MB solution in the presence PS and 5 wt% CoO@meso-CN catalyst. Two main absorbance peaks are observed. The peak at 292 nm is ascribed to the  $\pi\to\pi^*$  transition related to unsaturated conjugate aromatic rings (Hung et al., 2016). The absorption peak at 664 nm is attributed to the chromophores functional groups of MB and its dimers, namely —C=S and —C=N, which may undergo hemolytic cleavage (Devi et al., 2009). Note that both absorption peaks at 292 and 664 nm rapidly decrease with an increase in reaction time and almost disappear at the end of 15 min of reaction time. The rapid attenuation of the peak at 664 nm, indicates the breakup of the characteristic color of the conjugate structure in MB molecule. The disappearance of absorbance at 292 nm is attributed to the degradation of aromatic fragments of MB and its intermediates.

To gain further insights into the catalytic activity of CoO@meso-CN toward different types of dyes, degradation experiments were performed by selecting methyl red (MR) and methyl orange (MO) as neutral and anionic dyes, respectively, as shown in Fig. S5. Under the same reaction conditions, the removal efficiency of MB, MR, and MO is 99, 96, and 72% after 15 min of reaction, respectively, (Fig. S5a). It is evident that the lesser amounts of MR (7%) and MO (2%) adsorbed compared with that of MB (20%) in the dark can be due to the surface charge of CoO@meso-CN (Mohamed et al., 2018). Several studies have depicted that the catalytic degradation is a surface-mediated process and the catalytic efficiency and rate is highly dependent on the adsorption of organic dyes onto the surface of catalyst (Shaban et al., 2018; Abukhadra et al., 2018a, 2018b (1, 2)). In order to explore this aspect, we have

determined pH $_{\rm pzc}$  of CoO@meso-CN with the value of 4.17, which means that CoO@meso-CN possesses the negative charge at pH 7 (Fig. S5b) and preferentially adsorbs cationic MB, resulting in excellent degradation efficiency and rate compared to neutral MR and anionic MO. Based on the Langmuir isotherm model, the calculated maximum adsorption capacity of MB is much higher than that of MR and MO (Fig. S5c). Furthermore, in order to assess the degradation of these dyes in terms of mineralization, TOC analysis of the dye samples at the end of 15 min was performed. The order of rate constant and mineralization of the dyes follows MB > MR > MO (Fig. S5d). Therefore, MB is selected for all the following experiments because of the excellent catalytic degradation efficiency and rate.

It is known that the PS activation by CoO@meso-CN is an electron transfer process by which free radical is generated. Therefore, electrochemical impedance spectroscopy (EIS) is carried out to investigate the electron transfer resistance as affected by the amount of CoO NPs doped on meso-CN to further study the catalytic reaction of PS activation. The experimental Nyquist, shown in Fig. 4d reflects the reaction on the surface of the electrode. A smaller arc radius means a more facile charge transfer process at the electrode-water interface (Nguyen et al., 2019). Obviously, CoO@meso-CN composites show a smaller arc radius than that of the pristine meso-CN, suggesting that CoO@meso-CN has a stronger electronic conductivity and would be beneficial for PS activation. Tang et al. (2018) fabricated mesoporous carbon (CMK) activating PS for degradation of organic pollutants and found that low resistance of CMK confirmed by ESI plot could accelerate oxidation reaction via fast electron transfer on CMK surface. In our result, the 5 wt% CoO@meso-CN shows the smallest arc radius ( $R_{CT}=2.64~k\Omega$ ) in comparison with the other CoO@meso-CN catalysts, which demonstrates that the result of EIS analysis is consistent with that of MB degradation by different CoO loading CoO@meso-CN composites. This suggests that the fast electron transfer greatly accelerates the oxidation reaction in the removal efficiency and rate of MB over the CoO@meso-CN catalyzed PS system.



**Fig. 4.** Effect of different catalysts on activation of PS for (a) MB degradation, and (b) TOC removal. (c) Time-dependent UV-vis absorption spectra of MB, and (d) Nyquist plot (Reaction conditions: [MB] = 0.1 mM, [PS] = 20 mM, [catalyst] = 0.2 g L<sup>-1</sup>, pH =  $7.0 \pm 0.1$ , T = 25 °C).

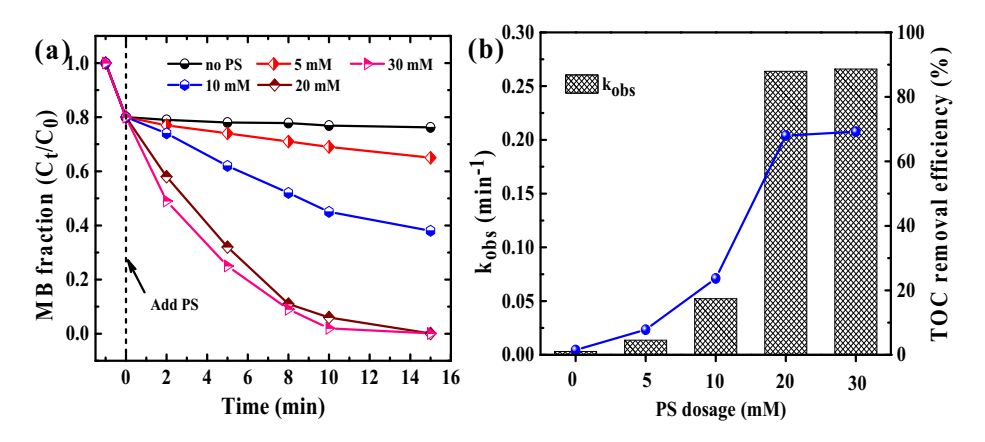


**Fig. 5.** Effect of PS dosage on activation of PS for (a) MB degradation, and (b) TOC removal. (Reaction conditions: [MB] = 0.1 mM, [PS] = 0-30 mM, [catalyst] = 0.2 g L<sup>-1</sup>, pH =  $7.0 \pm 0.1$ , T = 25 °C).

### 3.3. Effect of initial PS dosage on the catalytic activity on MB degradation

Fig. 5a shows the effect of PS concentration on MB degradation in the presence of 5 wt% CoO@meso-CN. In the absence of PS, MB removal is about 23.8% attributed to adsorption. In the presence of 0.2 g  $L^{-1}$ CoO@meso-CN catalyst, MB removal significantly is enhanced from 35 to >99% in 15 min when the PS dosage is increased from 5 to 20 mM, which is mainly brought by the production of more reactive radicals (Dong et al., 2017b). However, when the amount of PS further increases up to 30 mM, no remarkable change in removal efficiency is observed compared to 20 mM PS due to the self-quenching effect because of excessive radicals (Dong et al., 2018b). The k<sub>obs</sub> for MB is increased from 0.013 to  $0.264 \, \text{min}^{-1}$  and limited enhancement is observed when PS dosage increases to 30 mM (0.266 min<sup>-1</sup>). A similar phenomenon is also observed in TOC removal, the high removal TOC efficiency of 68% is achieved at 20 mM PS; whereas excessive PS (30 mM) only can slightly improve the efficiency by mere 1.2% (Fig. 5b). Furthermore, a linear relationship can be established between k<sub>obs</sub> (min<sup>-1</sup>) and PS dosage in the range of 5-20 mM, which indicates that the availability of PS is the limiting factor affecting the production of radicals at a low PS dose and the PS contribution become considerably less important with further increase in PS concentration beyond a certain value, e.g., 20 mM. A PS concentration at 20 mM is selected for further experiments.

### 3.4. Effect of initial pH on the catalytic degradation of MB

It is reported that  $SO_4^{\bullet-}$  based AOPs can work in a wide range pH compared to conventional Fenton oxidation process (Anipsitakis and

Dionysiou, 2003). Hence, the influence of initial pH on MB degradation is also studied at pH 3, 5, 7, 9, and 11, individually. Fig. 6a and b show the MB removal efficiency, k<sub>obs</sub>, and TOC of the CoO@meso-CN/PS process. Results show an increase in MB and TOC removal as the initial pH increases from 3 to 11. Especially, at the initial pH of 11, MB can be completely degraded in 10 min and the highest  $k_{obs}$  are 0.494 min<sup>-1</sup>. The adsorption capacity of CoO@meso-CN toward MB also increases with the increase in pH from 3 to 11. The difference in catalytic efficiency and adsorption are mainly caused by the catalytic reaction over the catalytic surface related to pH<sub>pzc</sub> of CoO@meso-CN. The pH<sub>pzc</sub> of CoO@meso-CN in this study is about 4.17 (Fig. S4) and MB is a cationic dye, so with the increase in pH to greater than  $pH_{pzc}$ , the adsorption of MB onto the negatively charged surface of CoO@meso-CN become stronger, which accelerates MB degradation. Additionally, under alkaline condition, more hydroxyl radicals are converted from sulfate radicals in accordance with the following reaction (Dong et al., 2018a):

$$SO_4^{-} + OH^- \rightarrow SO_4^{2-} + OH^-$$
 (1)

More importantly, the cobalt-leaching is dramatically suppressed at the basic condition, which is consistent with the highest stability of CoO@meso-CN. At initial pH 11, the lowest Co leaching of 15  $\mu g \ L^{-1} \ Co^{2+}$  is detected in the treated solution compared to 324  $\mu g \ L^{-1} \ Co^{2+}$  at initial pH 3, which indicates that basic condition is beneficial to protecting the surface crystallinity of CoO that not only effectively prevents metal ion leaching to the reaction solution but also facilitates the heterogeneous PS activation (Yao et al., 2013).

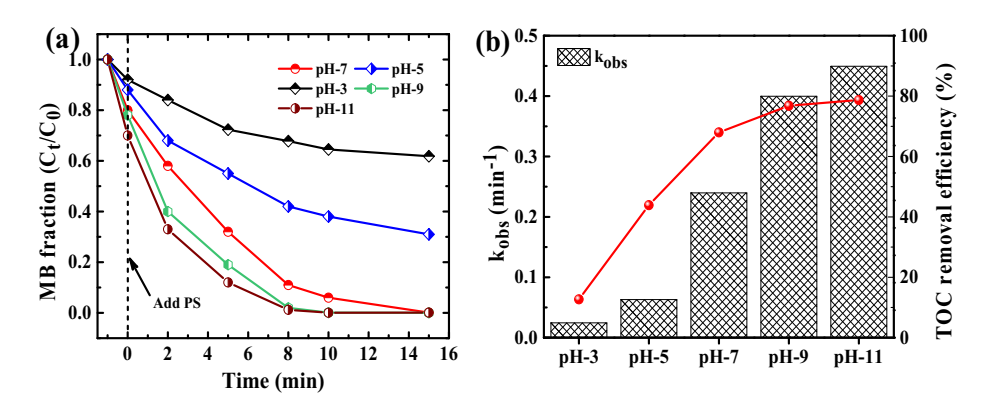


Fig. 6. Effect of pH on activation of PS for (a) MB degradation, and (b) TOC removal. (Reaction conditions: [MB] = 0.1 mM, [PS] = 0-30 mM, [catalyst] = 0.2 g L $^{-1}$ , pH =  $3-11 \pm 0.1$ , T = 25 °C).

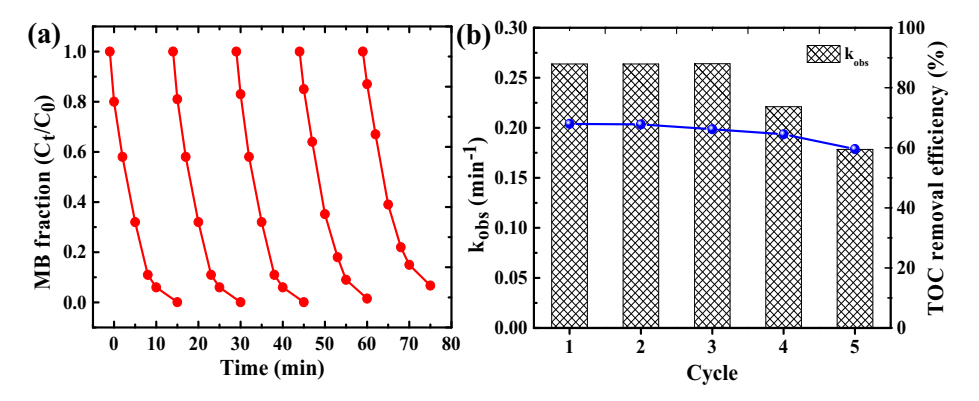


Fig. 7. Recyclability experiments on activation of PS for (a) MB degradation, and (b) TOC removal (Reaction conditions: [MB] = 0.1 mM, [PS] = 20 mM, [catalyst] = 0.2 g L<sup>-1</sup>, pH = 7.0 ± 0.1, T = 25 °C).

### 3.5. Stability and reusability of CoO@meso-CN

Fig. 7 shows the performance of the CoO@mesoCN catalyst in multiple cycles. The stability and reusability of CoO@meso-CN are examined in 5 repeated injections of 0.1 mM MB each into the solution at pH 7. It is apparent that the catalytic activity of CoO@meso-CN is excellent with a near complete MB removal after 5 continuously operation cycles (Fig. 7a), suggesting that the CoO@meso-CN composite possesses high stability and can be used repeatedly for the treatment of MB. The reaction rate of MB degradation almost remains unchanged during the first 3 cycles at 0.263 min<sup>-1</sup> and then decreases slightly from  $0.263 \,\mathrm{min^{-1}}$  to  $0.178 \,\mathrm{min^{-1}}$  at the 5th cycle (Fig. 7b). TOC removal efficiency slightly decreases in 5 cycles (from 68% to 59.6%). The slight decrease in k<sub>obs</sub> may be caused by the adsorbed intermediates at the active CoO site of CoO@meso-CN (Nguyen and Doong, 2017). On the other hand, the concentration of leached cobalt, detected by ICP-AES, is in the range of 17–23  $\mu$ g L<sup>-1</sup>, which is acceptable according to the international water quality standard of Co (50  $\mu$ g L<sup>-1</sup>). In order to evaluate the toxicity variation during the MB degradation process, V. fischeri inhibition test was undertaken by using Mictotox® at different cycles. The analyses of the sample treated with CoO@meso-CN reveals that a clear decrease in the toxicity of the dye is achieved at the end of each cycle and the inhibition percentage is lower than 5% (Fig. S6). Hence, it can be concluded that MB is effectively eliminated without acute toxicity to the test organism. Moreover, the XRD pattern of CoO@meso-CN before and after five consecutive cycles is almost identical (Fig. S7). The above results demonstrate clearly that CoO@meso-CN composite is environmentally friendly and structurally stable with high catalysis efficiency and recyclability.

### 3.6. Catalytic reaction mechanism in CoO@meso-CN/PS process

To further identify the main oxidative species in the CoO@meso-CN/ PS system, free radical quenching experiments and EPR spectroscopy combined with DMP as the spin trapping agent are utilized to investigate the effect of radicals. It has been reported that two different reactive oxidants (SO<sub>4</sub>• and OH•) are often generated for the catalystmediated decomposition of PS (Azhar et al., 2018). Generally, tertbutanol (tBuOH) is used as an effective quencher for OH• with high rate constant of  $8.0 \times 10^5 \,\mathrm{M}^{-1} \,\mathrm{s}^{-1}$ , while methanol (MeOH) can capture both  $SO_4^{\bullet-}$  and  $OH^{\bullet}$  with a rate constant of  $2.5 \times 10^7$  and 9.7 $\times$  10<sup>8</sup> M<sup>-1</sup> s<sup>-1</sup>, respectively (Indrawirawan et al., 2015). Based on the above information, quenching experiments with excessive tBuOH and MeOH allow the distinction of the extent of contribution to reactions between SO<sub>4</sub>• and OH•. As illustrated in Fig. 8a, the application of both MeOH and tBuOH with a high concentration (50 mM) can significantly inhibit the degradation of MB. The degradation efficiency decreases from 99% in the absence of scavenger to 67% and 57% after 15 min in the presence of MeOH and tBuOH, respectively. In addition, the corresponding k<sub>obs</sub> for MB degradation decline from 0.263 min<sup>-1</sup> in the absence of scavenger to 0.059 min<sup>-1</sup> and 0.040 min<sup>-1</sup> in the presence of MeOH and tBuOH, respectively. Based on the quenching results between MeOH and tBuOH, it can be clearly suggested that both the SO<sub>4</sub>• and OH• are a presence in the CoO@meso-CN/PS process and that OH• contributes to the degradation of MB at a greater extent than  $SO_4$ •

In order to further validate the reaction mechanism in the CoO@ meso-CN/PS system, EPR analysis using 5, 5-dimethylpyrroline-oxide DMPO as spin trapping agent is conducted to monitor the radical

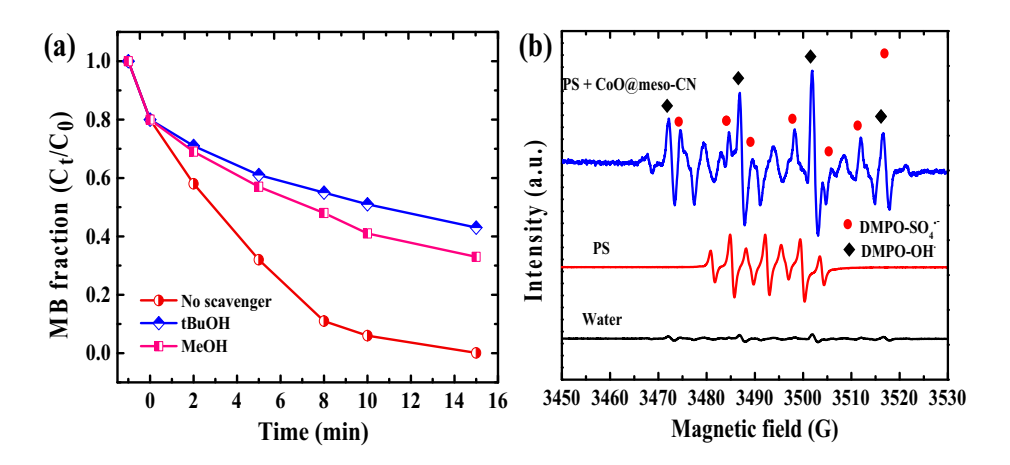


Fig. 8. EPR spectra of DMPO adducts, and (b) effect of scavengers on MB degradation (reaction conditions: [MB] = 0.1 mM, [PS] = 20 mM, [catalyst] = 0.2 g L<sup>-1</sup>, pH =  $7.0 \pm 0.1$ , T = 25 °C).

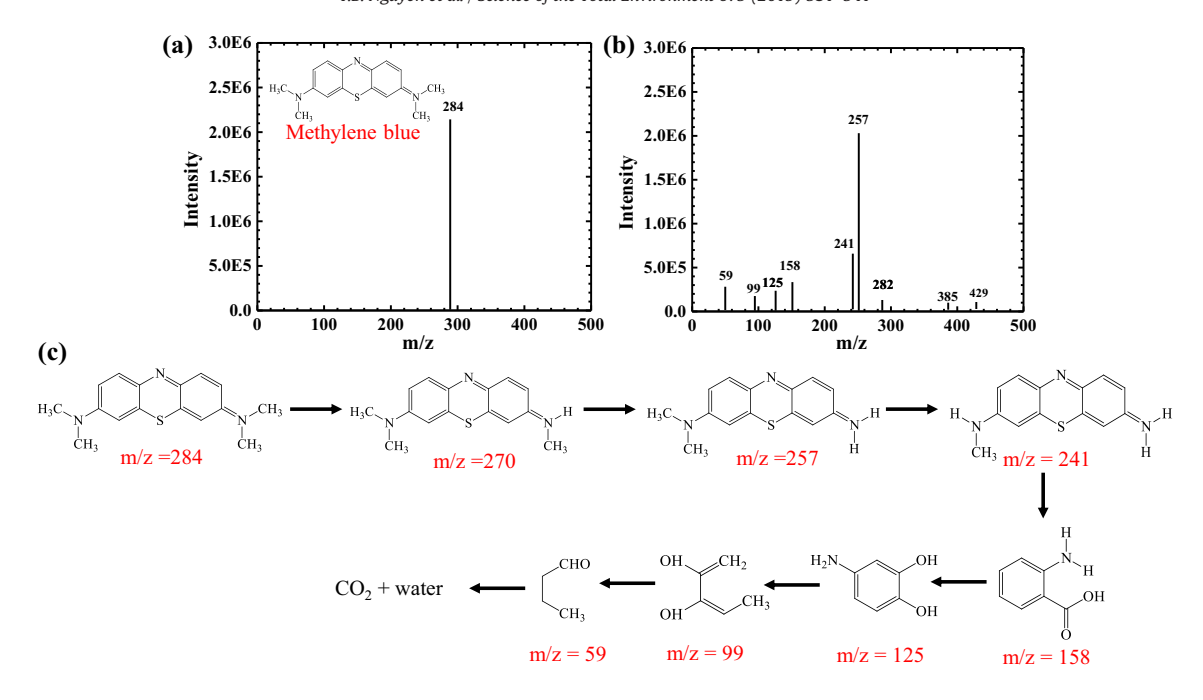


Fig. 9. Proposed degradation pathway of MB by CoO@meso-CN activated persulfate.

revolution. As depicted in Fig. 8b, no peaks are identified for pure water with the addition of DMPO (i.e., control), which suggests that no spins are captured. In contrast, characteristic signals of 5,5-dimethlprroline-(2)-oxyl-(1) (DMPOX) with an intensity ratio of 1:2:1:2:1 are identified with the addition of DMPO to the PS solution. The EPR spectrum obtained is assigned to 5,5-dimethyl-1-pyrrolidone-2-oxyl (DMPOX) originated from the oxidation of DMPO by PS. The patterns of the hyperfine splitting are consistent with those of DMPOX reported in the literature ( $\alpha_N = 7.3$  and  $\alpha_H = 3.9$ ) (Lee et al., 2015). When CoO@meso-CN is added together with DMPO and PS, both DMPO-OH and DMPO-SO<sub>4</sub> are detected. The peaks with four lines of 1:2:2:1 could be assigned to DMPO-OH adduct (with hyperfine splitting constants of  $\alpha_H = \alpha_N =$ 14.9 G), which implies the reaction of DMPO with OH• radicals (Nguyen et al., 2019). Meanwhile, the pattern of  $SO_4^{\bullet-}$  product ( $\alpha_N =$ 13.2 G,  $\alpha_H = 9.6$  G,  $\alpha_H = 1.48$  G,  $\alpha_H = 0.78$  G) is consistent with those of DMPO-SO<sub>4</sub> reported in the literature (Shah et al., 2019), but the intensity of DMPO-SO<sub>4</sub> signals is weaker than that of DMPO-OH due to the fast transformation from DMPO-SO<sub>4</sub> to DMPO-OH via nucleophilic substitution (Timmins et al., 1999). Overall, the EPR results sufficiently confirm the production of both radicals responsible for MB degradation during the catalytic reaction.

# 3.7. Degradation pathway of MB in the CoO@meso-CN/PS system

HPLC/MS/MS is used to identify the intermediates during the reaction and to establish the pathway of MB degradation in the CoO@meso-CN/PS system. Fig. 9a shows a high intense single peak of at m/z = 284 ascribed to the parent MB molecule. After 15 min, no MB is observed and the occurrence of new peaks attributed to the production of intermediates shown in Fig. 9b. Based on the intermediate products identified, a possible degradation pathway of MB by the CoO@meso-CN/PS system is proposed primarily, as given in Fig. 9c. Initially, the SO<sub>4</sub>• and OH• preferentially attacks the chromophore center of the dye molecule, with the demethylation cleavage and release of one or more of the methyl group substituents on the amine groups, leading to the formation of azure A (m/z = 256), B (m/z = 270), and C (m/z = 241) (Hisaindee et al., 2013). Finally, the breakdown of aromatic rings takes place and the resultant smaller intermediates subsequently undergo successive degradation reactions to yield carbon dioxide and water, resulting in a decrease in TOC concentration. Thus, HPLC-MS/MS results strongly confirm catalytic degradation and mineralization of MB dye by •OH and other reactive species produced by the catalyst.

### 4. Conclusion

We have demonstrated a simple and facile synthesis method for the fabrication of CoO@meso-CN nanocomposite with various CoO loadings, and the first use of the catalyst to activate PS for MB degradation. The small CoO NPs with an average diameter of 10 nm is highly dispersed and anchored firmly on the functional moieties of meso-CN surface, which helps the formation of the particle by in situ reduction and avoids the agglomeration of particles on the porous surface. Furthermore, the interfacial interactions between the ultrafine CoO NPs and meso-CN, create a high surface area, regular mesopores, graphitic nature of the meso-CN support, can further enhance the catalytic activation of PS for MB degradation. Among all catalysts studied, the 5-wt% CoO@ meso-CN exhibits the best catalyst performance with kobs of 0.264 min<sup>-1</sup> for MB degradation in the presence of PS. High initial pH, specifically at pH 11, is more beneficial for the activation of PS. Noticeably, the CoO@meso-CN nanocatalyst is highly stable with consistently high degree of MB degradation and negligible cobalt leaching for at least 5 consecutive catalytic cycles. Both SO<sub>4</sub>• and OH• are proved to be the major reactive species according to EPR and quenching experiments. The degradation intermediates of MB during the catalytic reaction are also identified by HPLC/MS/MS and the possible degradation pathway is proposed. Hence, the combination of CoO nanoparticles and meso-CN is a promising green chemistry approach with great potential applications for catalytic degradation of hazardous chemicals.

### Acknowledgments

The authors wish to thank the Ministry of Science and Technology, Taiwan (MOST), for generous financial support under grant no. 106-2221-E-002-002-MY3. Addition support was provided by US NSF IOA (1632899) to CPH.

# Appendix A. Supplementary data

Supplementary data to this article can be found online at https://doi.org/10.1016/j.scitotenv.2019.04.230.

### References

- Abukhadra, M.R., Shaban, M., El Samad, M.A.A., 2018a. (1). Enhanced photocatalytic removal of Safranin-T dye under sunlight within minute time intervals using heulandite/polyaniline@ nickel oxide composite as a novel photocatalyst. Ecotoxicol. Environ. Saf. 162. 261–271.
- Abukhadra, M.R., Shaban, M., Sayed, F., Saad, I., 2018b. (2). Efficient photocatalytic removal of safranin-O dye pollutants from water under sunlight using synthetic bentonite/polyaniline@Ni<sub>2</sub>O<sub>3</sub> photocatalyst of enhanced properties. Environ. Sci. Pollut. Res. 25 (33), 33264–33276.
- Al-Anazi, A., Abdelraheem, W.H., Han, C., Nadagouda, M.N., Sygellou, L., Arfanis, M.K., Falaras, P., Sharma, V.K., Dionysiou, D.D., 2018. Cobalt ferrite nanoparticles with controlled composition-peroxymonosulfate mediated degradation of 2-phenylbenzimidazole-5-sulfonic acid. Appl. Catal. B Environ. 221, 266–279.
- Anipsitakis, G.P., Dionysiou, D.D., 2003. Degradation of organic contaminants in water with sulfate radicals generated by the conjunction of peroxymonosulfate with cobalt. Environ. Sci. Technol. 37, 4790–4797.
- Azhar, M.R., Vijay, P., Tade, M.O., Sun, H.Q., Wang, S.B., 2018. Submicron sized water-stable metal organic framework (bio-MOF-11) for catalytic degradation of pharmaceuticals and personal care products. Chemosphere 196, 105–114.
- Bello, M., Zaidi, S.M.J., Al-Ahmed, A., Basu, S., Park, D.H., Lakhi, K.S., Vinu, A., 2017. Pt-Ru nanoparticles functionalized mesoporous carbon nitride with tunable pore diameters for DMFC applications. Microporous Mesoporous Mater. 252, 50–58.
- Bindumadhavan, K., Yeh, M.H., Chou, T.C., Chang, P.Y., Doong, R.A., 2016. Ultrafine CoO embedded reduced graphene oxide nanocomposites: a high rate anode for Li–ion battery. ChemistrySelect 1 (18), 5758–5767.
   Chen, C.-F., Binh, N.T., Chen, C.-W., Dong, C.-D., 2015a. Removal of polycyclic aromatic hy-
- Chen, C.-F., Binh, N.T., Chen, C.-W., Dong, C.-D., 2015a. Removal of polycyclic aromatic hydrocarbons from sediments using sodium persulfate activated by temperature and nanoscale zero-valent iron. J. Air Waste Manag. Assoc. 65, 375–383.
- Chen, C.W., Binh, N.T., Hung, C.M., Chen, C.F., Dong, C.D., 2015b. Removal of polycyclic aromatic hydrocarbons from sediments using chemical oxidation processes. J. Adv. Oxid. Technol. 18, 15–22.
- Datta, K.K.R., Reddy, B.V.S., Ariga, K., Vinu, A., 2010. Gold nanoparticles embedded in a mesoporous carbon nitride stabilizer for highly efficient three-component coupling reaction. Angew. Chem. Int. Ed. 49, 5961–5965.
- Devi, L.G., Murthy, B.N., Kumar, S.G., 2009. Heterogeneous photo catalytic degradation of anionic and cationic dyes over TiO<sub>2</sub> and TiO<sub>2</sub> doped with Mo<sup>6+</sup> ions under solar light: correlation of dye structure and its adsorptive tendency on the degradation rate. Chemosphere 76, 1163–1166.
- Dhaka, S., Kumar, R., Khan, M.A., Paeng, K.J., Kurade, M.B., Kim, S.J., Jeon, B.H., 2017. Aqueous phase degradation of methyl paraben using UV-activated persulfate method. Chem. Eng. J. 321, 11–19.
- Dong, C.D., Chen, C.W., Hung, C.M., 2017a. Synthesis of magnetic biochar from bamboo biomass to activate persulfate for the removal of polycyclic aromatic hydrocarbons in marine sediments. Bioresour. Technol. 245, 188–195.
- Dong, C.D., Tsai, M.L., Chen, C.W., Hung, C.M., 2017b. Heterogeneous persulfate persulfate oxidation of BTEX and MTBE using  $Fe_3O_4$ -CB magnetite composites and the cytotoxicity of degradation products. Int. Biodeterior. Biodegradation 124, 109–118.
- Dong, C.D., Chen, C.W., Kao, C.M., Chien, C.C., Hung, C.M., 2018a. Wood-Biochar-supported magnetite nanoparticles for remediation of PAH-contaminated estuary sediment.
- Dong, C.D., Tsai, M.L., Chen, C.W., Hung, C.M., 2018b. Remediation and cytotoxicity study of polycyclic aromatic hydrocarbon-contaminated marine sediments using synthesized iron oxide-carbon composite. Environ. Sci. Pollut. Res. 25, 5243–5253.
- Dos Santos, S.M.L., Nogueira, K.A.B., Gama, M.D., Lima, J.D.F., da Silva, I.J., de Azevedo, D.C.S., 2013. Synthesis and characterization of ordered mesoporous silica (SBA-15 and SBA-16) for adsorption of biomolecules. Microporous Mesoporous Mater. 180, 284–292
- Elavarasan, S., Baskar, B., Senthil, C., Bhanja, P., Bhaumik, A., Selvam, P., Sasidharan, M., 2016. An efficient mesoporous carbon nitride (g-C<sub>3</sub>N<sub>4</sub>) functionalized Pd catalyst for carbon-carbon bond formation reactions. RSC Adv. 6, 49376–49386.
- Hisaindee, S., Meetani, M.A., Rauf, M.A., 2013. Application of LC-MS to the analysis of advanced oxidation process (AOP) degradation of dye products and reaction mechanisms. Trends Analyt. Chem. 49, 31–44.
- Hu, P., Long, M., 2016. Cobalt-catalyzed sulfate radical based advanced oxidation: a review on heterogeneous catalysis and application. Appl. Catal. B Environ. 181, 103–117.
- Hung, C.M., Chen, C.W., Liu, Y.Y., Dong, C.D., 2016. Decolorization of methylene blue by persulfate activated with FeO magnetic particles. Water Environ. Res. 88, 675–686.
- Indrawirawan, S., Sun, H.Q., Duan, X.G., Wang, S.B., 2015. Low temperature combustion synthesis of nitrogen-doped graphene for metal-free catalytic oxidation. J. Mater. Chem. A 3, 3432–3440.
- Jaafarzadeh, N., Ghanbari, F., Ahmadi, M., 2017. Efficient degradation of 2,4-dichlorophenoxyacetic acid by peroxymonosulfate/magnetic copper ferrite nanoparticles/ozone: a novel combination of advanced oxidation processes. Chem. Eng. J. 320, 436–447.
- Jun, Y.S., Hong, W.H., Antonietti, M., Thomas, A., 2009. Mesoporous, 2D hexagonal carbon nitride and titanium nitride/carbon composites. Adv. Mater. 21, 4270.
- Kahri, H., Sevim, M., Metin, O., 2017. Enhanced catalytic activity of monodispersed AgPd alloy nanoparticles assembled on mesoporous graphitic carbon nitride for the hydrolytic dehydrogenation of ammonia borane under sunlight. Nano Res. 10, 1627–1640.
- Khan, M.R., Khan, M.A., Alothman, Z.A., Alsohaimi, I.H., Naushad, M., Al-Shaalan, N.H., 2014. Quantitative determination of methylene blue in environmental samples by solid-phase extraction and ultra-performance liquid chromatography-tandem mass spectrometry: a green approach. RSC Adv. 4, 34037–34044.

- Kroke, E., Schwarz, M., Horath-Bordon, E., Kroll, P., Noll, B., Norman, A.D., 2002. Tri-s-triazine derivatives. Part I. From trichloro-tri-s-triazine to graphitic C<sub>3</sub>N<sub>4</sub> structures. New I. Chem. 26, 508–512.
- Kwon, K., Sa, Y.J., Cheon, J.Y., Joo, S.H., 2012. Ordered mesoporous carbon nitrides with graphitic frameworks as metal-free, highly durable, methanol-tolerant oxygen reduction catalysts in an acidic medium. Langmuir 28, 991–996.
- Lakhi, K.S., Park, D.H., Al-Bahily, K., Cha, W., Viswanathan, B., Choy, J.H., Vinu, A., 2017.
  Mesoporous carbon nitrides: synthesis, functionalization, and applications. Chem.
  Soc. Rev. 46, 72–101
- Lee, Y.C., Lo, S.L., Kuo, J., Huang, C.P., 2013. Promoted degradation of perfluorooctanic acid by persulfate when adding activated carbon. J. Hazardous Materials 261, 463–469.
- Lee, H., Lee, H.J., Jeong, J., Lee, J., Park, N.B., Lee, C., 2015. Activation of persulfates by carbon nanotubes: oxidation of organic compounds by nonradical mechanism. Chem. Eng. J. 266, 28–33
- Leyssens, L., Vinck, B., Van Der Straeten, C., Wuyts, F., Maes, L., 2017. Cobalt toxicicy in humans—a review of the potential sources and systemic health effects. Toxicology 387, 43–56
- Li, X.B., Masters, A.F., Maschmeyer, T., 2015. Photocatalytic hydrogen evolution from silica-templated polymeric graphitic carbon nitride—is the surface areai mportant? Chemcatchem 7, 121–126.
- Lominchar, M.A., Santos, A., de Miguel, E., Romero, A., 2018. Remediation of aged diesel contaminated soil by alkaline activated persulfate. Sci. Total Environ. 622, 41–48.
- Mane, G.P., Talapaneni, S.N., Lakhi, K.S., Ilbeygi, H., Ravon, U., Al-Bahily, K., Mori, T., Park, D.H., Vinu, A., 2017. Highly ordered nitrogen-rich mesoporous carbon nitrides and their superior performance for sensing and photocatalytic hydrogen generation. Angew. Chem. Int. Ed. 56, 8481–8485.
- Mohamed, F., Abukhadra, M.R., Shaban, M., 2018. Removal of safranin dye from water using polypyrrole and nanofiber/Zn-Fe layered double hydroxide nanocomposite (PPy NF/Zn-Fe-LDH) of enhanced adsorption and photocatalytic properties. Sci. Total Environ. 640. 352–363.
- Nguyen, T.B., Doong, R.A., 2017. Heterostructured ZnFe<sub>2</sub>O<sub>4</sub>/TiO<sub>2</sub> nanocomposites with a highly recyclable visible-light-response for bisphenol A degradation. RSC Adv. 7, 50006–50016.
- Nguyen, T.B., Huang, C.P., Doong, R.A., 2019. Photocatalytic degradation of bisphenol A over a ZnFe<sub>2</sub>O<sub>4</sub>/TiO<sub>2</sub> nanocomposite under visible light. Sci. Total Environ. 646, 745–756
- Olmez-Hanci, T., Arslan-Alaton, I., 2013. Comparison of sulfate and hydroxyl radical based advanced oxidation of phenol. Chem. Eng. J. 224, 10–16.
- Rastogi, A., Ai-Abed, S.R., Dionysiou, D.D., 2009. Sulfate radical-based ferrousperoxymonosulfate oxidative system for PCBs degradation in aqueous and sediment systems. Appl. Catal. B Environ. 85, 171–179.
- Shaban, M., Ashraf, A.M., Abukhadra, M.R., 2018. TiO<sub>2</sub> nanoribbons/carbon nanotubes composite with enhanced photocatalytic activity: Fabriation, characterization, and application. Sci. Rep. 8 (1), 781.
- Shah, N.S., Khan, J.A., Sayed, M., Khan, Z.U., Ali, H.S., Murtaza, B., Khan, H.M., Imran, M., Muhammad, N., 2019. Hydroxyl and sulfate radical mediated degradation of ciprofloxacin using nano zerovalent manganese catalyzed  $S_2O_8^{2-}$ . Chem. Eng. J. 356, 199–209.
- Shih, Y.J., Binh, N.T., Chen, C.W., Chen, C.F., Dong, C.D., 2016. Treatability assessment of polycyclic aromatic hydrocarbons contaminated marine sediments using permanganate, persulfate and Fenton oxidation processes. Chemosphere 150, 294–303.
- Shukla, P., Sun, H.Q., Wang, S.B., Ang, H.M., Tade, M.O., 2011. Co-SBA-15 for heterogeneous oxidation of phenol with sulfate radical for wastewater treatment. Catal. Today 175, 380-385.
- Tang, L., Liu, Y., Wang, J., Zeng, G., Deng, Y., Dong, H., Feng, H., Wang, J., Peng, B., 2018. Enhanced activation process of persulfate by mesoporous carbon for degradation of aqueous organic pollutants: electron transfer mechanism. Appl. Catal.s B Environ. 231 (1-10)
- Timmins, G.S., Liu, K.J., Bechara, E.J.H., Kotake, Y., Swartz, H.M., 1999. Trapping of free radicals with direct in vivo EPR detection: a comparison of 5,5-dimethyl-1-pyrroline-Noxide and 5-diethoxyphosphoryl-5-methyl-1-pyrroline-Noxide as spin traps for HO• and SO<sub>4</sub>. Free Rad. Biol. Med. 27, 329–333.
- Vinu, A., 2008. Two-dimensional hexagonally-ordered mesoporous carbon nitrides with tunable pore diameter, surface area and nitrogen content. Adv. Funct. Mater. 18, 816–827.
- Yang, Q., Choi, H., Al-Abed, S.R., Dionysiou, D.D., 2009. Iron-cobalt mixed oxide nanocatalysts: heterogeneous peroxymonosulfate activation, cobalt leaching, and ferromagnetic properties for environmental applications. Appl. Catal. B Environ. 88, 462-469.
- Yang, G., Tang, L., Zeng, G., Tang, J., Pang, Y., Zhou, Y., Liu, Y., Wang, J., Zhang, S., Xiong, W., 2015. Simultaneous removal of lead and phenol contamination from water by nitrogen-functionalized magnetic ordered mesoporous carbon. Chem. Eng. J. 259, 845–864.
- Yao, Y., Xu, C., Qin, J., Wei, F., Rao, M., Wang, S., 2013. Synthesis of magnetic cobalt nanoparticles anchored ongraphene nanosheets and catalytic decomposition of orange II. Ind. Eng. Chem. Res. 52 (49), 17341–17350.
- Zhang, J., Chen, M.Y., Zhu, L., 2016. Activation of persulfate by Co<sub>3</sub>O<sub>4</sub> nanoparticles for orange G degradation. RSC Adv. 6, 758–768.
- Zhao, Z.K., Dai, Y.T., Lin, J.H., Wang, G.R., 2014. Highly-ordered mesoporous carbon nitride with ultrahigh surface area and pore volume as a superior dehydrogenation catalyst. Chem. Mater. 26. 3151–3161.